



Modification of NiO_x hole transport layers with 4-bromobenzylphosphonic acid and its influence on the performance of lead halide perovskite solar cells

Jimmy Mangalam¹ · Thomas Rath¹ · Stefan Weber¹ · Birgit Kunert² · Theodoros Dimopoulos³ · Alexander Fian⁴ · Gregor Trimmel¹

Received: 8 March 2019 / Accepted: 6 April 2019 / Published online: 16 April 2019
© The Author(s) 2019

Abstract

Lead halide perovskites have proved to be exceptionally efficient absorber materials for photovoltaics. Besides improving the properties of the perovskite absorbers, device engineering and the optimization of interfaces will be equally important to further the advancement of this emerging solar cell technology. Herein, we report a successful modification of the interface between the NiO_x hole transport layer and the perovskite absorber layer using 4-bromobenzylphosphonic acid based self-assembled monolayers leading to an improved photovoltaic performance. The modification of the NiO_x layer is carried out by dip coating which allows sufficient time for the self-assembly. The change in the surface free energy and the non-polar nature of the resulting surface is corroborated by contact angle measurements. X-ray photoelectron spectroscopy confirms the presence of phosphor and bromine on the NiO_x surface. Furthermore, the resultant solar cells reveal increased photovoltage. For typical devices without and with modification, the photovoltage improves from 0.978 V to 1.029 V. The champion V_{OC} observed was 1.099 V. The increment in photovoltage leads to improved power conversion efficiencies for the modified cells. The maximum power point tracking measurements of the devices show stable power output of the solar cells.

1 Introduction

Lead halide perovskite solar cells have reached certified power conversion efficiencies (PCEs) greater than 23% in a conventional n-i-p architecture [1–3]. Similarly, also with perovskite solar cells based on a planar inverted p-i-n architecture efficiencies greater than 20% have imposingly been realized [4, 5]. In addition, devices in inverted p-i-n architecture have piqued considerable interest as they offer the possibility to be processed at low temperature and also on

flexible substrates [5–7]. The diminishing gap between the performance of both device architectures has been majorly possible due to optimizing the inorganic hole transport layers (HTLs). In particular, nickel oxide (NiO_x) films proved to be promising, as they allow facile processing, good stability and efficient hole extraction [8, 9]. Furthermore, different doping procedures for NiO_x such as incorporation of copper, cesium or silver ions have led to improved device performance and are opening up pathways for further optimisations [10–12].

In recent practice, the NiO_x layers for the application in perovskite solar cells are deposited majorly via solution processes by using sol–gel methods or nanoparticle dispersions in water [10, 13–19]. Moreover, atomic layer deposition, flame spray synthesis, pulsed laser deposition, sputtering and electrodeposition have been applied for the formation of NiO_x thin films [20–25].

In photovoltaics, interface engineering between charge transport layers and the absorber layer is an important approach in device optimization. One of the primary concepts utilized to achieve such engineering is the application of self-assembled monolayers (SAMs) [26–28]. The formation of a monolayer and the effective dipole of the applied

✉ Thomas Rath
thomas.rath@tugraz.at

¹ Institute for Chemistry and Technology of Materials (ICTM), NAWI Graz, Graz University of Technology, Stremayrgasse 9, 8010 Graz, Austria

² Institute of Solid State Physics, NAWI Graz, Graz University of Technology, Petersgasse 16, 8010 Graz, Austria

³ AIT Austrian Institute of Technology, Center for Energy, Photovoltaic Systems, Giefinggasse 4, 1210 Vienna, Austria

⁴ Joanneum Research Forschungsgesellschaft mbH, Franz-Pichler-Straße 30, 8160 Weiz, Austria

molecules can be explored for designing the properties at the aforementioned interface. The SAMs allow the manipulation of the work function and the wettability of the metal oxide films, and they can also passivate the interface [29, 30]. For example, Wang et al. reported on the effects of para-substituted benzoic acid SAMs on the NiO_x and perovskite interface. They highlighted an improved open circuit voltage (V_{OC}) due to the introduction of bromobenzoic acid (dipole moment of 2.1 D) as a monolayer on the NiO_x film [31].

In this work, we discuss the influence of the modification of the NiO_x HTL with 4-bromobenzylphosphonic acid (Br-BPA) on lead halide perovskite solar cells. We chose phosphonic acids as the interface modifier as they have so far been barely investigated in perovskite solar cells even though they have been thoroughly studied in organic field effect transistors as well as organic photovoltaics and possess beneficial properties for surface modification of metal oxides [32]. In a study on the modification of zinc oxide (ZnO) with benzylphosphonic acids (BPA), Lange et al. reported that BPA SAMs have a preferential tridentate binding on a ZnO surface. A tridentate binding suggests a stronger chemisorption of the SAM molecules on the metal oxide surface in comparison to the mono- and bi-dentate binding [32–35]. As absorber layer for the solar cells prepared in p-i-n architecture, a triple cation based perovskite with the composition $\text{Cs}_{0.1}(\text{FA}_{0.83}\text{MA}_{0.17})_{0.9}\text{Pb}(\text{I}_{0.83}\text{Br}_{0.17})_3$, introduced by Saliba et al. [36], was selected.

2 Experimental

2.1 Sample and solar cell preparation

All chemicals and solvents were used as purchased without any further purification. Nickel(II) nitrate hexahydrate and sodium hydroxide was purchased from Fluka and VWR, respectively. Lead iodide, lead bromide, formamidine iodide and PC₆₀BM were purchased from TCI, Alfa Aesar, GreatCell Solar and Solenne, respectively. The other chemicals used in this study, including the phosphonic acid molecule, and all the solvents were purchased from Merck (Sigma Aldrich).

2.2 Material synthesis

2.2.1 Synthesis and characterization of nickel oxide nanoparticles

The synthesis of the NiO_x nanoparticles was performed according to previous reports [15, 37–39]. In brief, nickel (II) nitrate hexahydrate ($\text{NiNO}_3 \cdot 6 \text{H}_2\text{O}$) (0.05 mol) was dispersed in 10 mL deionized water and stirred for 5 min. Afterwards sodium hydroxide (NaOH, 10 mmol/mL) was

added dropwise to adjust a pH of 10, which results in a colour change from dark to light green. The colloidal precipitate was then washed with deionized water to remove side products. The light green residue was further dried at 80 °C for 6 h followed by calcination at 270 °C for 2 h. This resulted in non-stoichiometric black nickel (II) oxide nanoparticles. The X-ray diffraction (XRD) pattern of the NiO_x nanoparticles is very similar to as reported in Ref. [15] and reveals reflections at 37.2°, 43.2°, 62.7°, 75.4° and 79.3° 2 θ , which correspond to the (111), (200), (220), (311), and (222) lattice planes in a cubic crystal structure. An estimation of the primary crystallite size based on the peak broadening via Scherrer formula led to a value of approx. 8 nm. For the preparation of the NiO_x ink, 20 mg/mL of the NiO_x nanoparticles were dispersed in deionized water. The ink was put in an ultrasonic bath for 2 h and then filtered using a 0.45 μm PVDF syringe filter.

2.3 Solar cell preparation

2.3.1 Glass/ITO substrates

Pre-patterned glass/ITO substrates ($15 \times 15 \times 1.1 \text{ mm}^3$) (15 Ω/sq) from Luminescence Technology Corp. (Lumtec) were carefully wiped using acetone before putting them into an isopropanol bath. The bath was further subjected to an ultrasonic bath for 10 min. The substrates were then dried using in an N_2 stream. Just before spin coating the NiO_x nanoparticle ink, the substrates were plasma etched using oxygen plasma for 3 min.

2.3.2 Preparation of the NiO_x films

The NiO_x nanoparticle ink was spin coated onto the glass/ITO substrates at a speed of 1000 rpm. Before the determination of the layer thickness and solar cell preparation, the films were allowed to dry in ambient conditions for 3 days. The as-prepared films revealed an average thickness distribution of ~25 nm.

2.3.3 Surface modification of the NiO_x films with Br-BPA

A 5 mmol/mL solution of Br-BPA was prepared in acetonitrile and was filtered using a 0.45 μm PVDF syringe filter. The application of the Br-BPA molecule was done by dip coating. In the dip coating method, the glass/ITO/ NiO_x substrates were dipped in the phosphonic acid solution for 1 min to allow adsorption. These substrates were then cleaned by dipping them in fresh acetonitrile solvent to allow removal of non-adsorbed phosphonic acid molecules from the modified surface. The substrates were then dried in an N_2 stream. The deposition was carried out in ambient conditions.

2.3.4 Preparation of the perovskite absorber layers

The cesium, formamidinium, and methylammonium based triple cation lead halide perovskite absorber layer was adapted from Saliba et al. [36]. The final composition chosen was $\text{Cs}_{0.1}(\text{FA}_{0.83}\text{MA}_{0.17})_{0.9}\text{Pb}(\text{I}_{0.83}\text{Br}_{0.17})_3$. The precursor solution consisted of 1 mmol/mL formamidinium iodide (FAI), 1.1 mmol/mL PbI_2 , 0.2 mmol/mL methylammonium bromide (MABr), and 0.2 mmol/mL PbBr_2 in a mixed dimethyl formamide (DMF)/dimethyl sulfoxide (DMSO) solvent with a 4:1 volume ratio. To this solution, 1.5 mmol/mL CsI in DMSO, was added to obtain a 10% Cs content. The final precursor solution was stirred overnight in inert conditions to allow sufficient reaction time. The solution was then filtered using a 0.45 μm PTFE syringe filter prior to spin coating. The perovskite absorber layer was spin coated on the non-modified and modified glass/ITO/ NiO_x substrates in a two-step spin coating process with 1000/6000 rpm for 10/20 s. In the last 5 s of spinning, chlorobenzene was dripped onto the substrate as an antisolvent. The substrates were annealed at 100 °C for 1 h. The thickness of the perovskite absorber layers was monitored using a Stylus profilometer and was found to be approximately 485 nm.

2.3.5 PC_{60}BM electron transport layer and top electrode

A phenyl- C_{61} -butyric acid methyl ester (PC_{60}BM) solution in chlorobenzene having a concentration of 20 mg/mL was prepared. The solution was stirred overnight and filtered using a 0.45 μm PTFE syringe filter prior to spin coating at 4000 rpm for 20 s. In a last step of the solar cell preparation, a 120 nm thick silver layer was deposited by thermal evaporation on top of the PC_{60}BM layer at an evaporation rate of 1–2 \AA s^{-1} using a shadow mask (0.09 cm^2).

2.4 Characterization techniques

XRD was performed on a PANalytical Empyrean system using $\text{Cu K}\alpha$ radiation. Ultraviolet–visible (UV–Vis) spectroscopy measurements were done using the UV–Vis Spectrometer—Lambda 35 by Perkin Elmer. The layer thicknesses were measured by surface profilometry using a DektakXT device by Bruker and the surface morphology of the perovskite films was characterized by scanning electron microscopy (SEM) images acquired on a Zeiss-Supra 40 scanning electron microscope with an in-lens detector and 5 kV acceleration voltage.

Contact angle measurements of the NiO_x films before and after the modification with Br-BPA were carried out on a Krüss DSA100 system using water and ethylene glycol as liquids. The surface free energy calculations were performed with the Owens-Wendt-Rabel & Kaelble method [40] using the Krüss Advance software.

X-ray photoelectron spectroscopy (XPS) measurements of the NiO_x and $\text{NiO}_x/\text{Br-BPA}$ SAM films were recorded using a multiprobe surface analysis system (Omicron Nanotechnology) equipped with a DAR 400 X-ray source (Al $\text{K}\alpha_1$ radiation, 1486.7 eV), an XM 500 quartz crystal monochromator (energy width: 0.15 eV), and an EA 125 hemispherical electron energy analyzer based on a 5-channel pulse counting channeltron.

The current density–voltage (JV) curves and maximum power point (MPP) tracking measurements of the solar cells were performed using a Keithley 2400 source meter and a LabView-based software inside a glove box (nitrogen atmosphere). For the JV curves, the scan rates were adjusted to 100 mVs^{-1} in the forward (fwd) direction (–0.02 V to 1.2 V) and backward (bwd) direction (1.2 V to –0.02 V) for both light and dark measurements. The illumination area was defined using a shadow mask (0.07 cm^2) and the light was provided by a Dedolight DLH500 lamp calibrated to an intensity of 100 mWcm^{-2} using a pyranometer from Kipp & Zonen. The External Quantum Efficiency (EQE) spectra were acquired using a MuLTImode 4 monochromator (Amko) equipped with a 75 W xenon lamp (LPS 210-U, Amko), a lock-in amplifier (Stanford Research Systems, Model SR830), and a Keithley 2400 source meter. The monochromatic light was chopped at a frequency of 30 Hz and the measurement setup was spectrally calibrated with a silicon photodiode (Newport Corporation, 818-UV/DB).

3 Results and discussion

The modification of the NiO_x thin films with Br-BPA was performed by dipping the films into an acetonitrile solution containing the Br-BPA molecules followed by washing the substrates in pure acetonitrile. A detailed description of the procedure can be found in the experimental part. The chemical structure of Br-BPA and a schematic illustration of the modification together with the used solar cell setup to investigate the influence of the modification on the photovoltaic performance are shown in Fig. 1a. During the dipping process, the phosphonic acid groups bind to the NiO_x surface whereby the Br-BPA molecules very likely form a SAM. Thereby, on the one hand the surface will become more non-polar due to the Br functionality which might influence wetting of the perovskite precursor solution and the crystallisation properties of the perovskite films. On the other hand, the Br-BPA molecule has a dipole moment of 2.3 D [33], which can facilitate charge extraction and also reduce the valence band energy of the NiO_x film, similar to as it was experimentally and theoretically shown for the modification of ZnO surfaces [30, 32, 34, 35].

As a first step, the presence of a Br-BPA SAM and the modification of the surface properties of the NiO_x films were

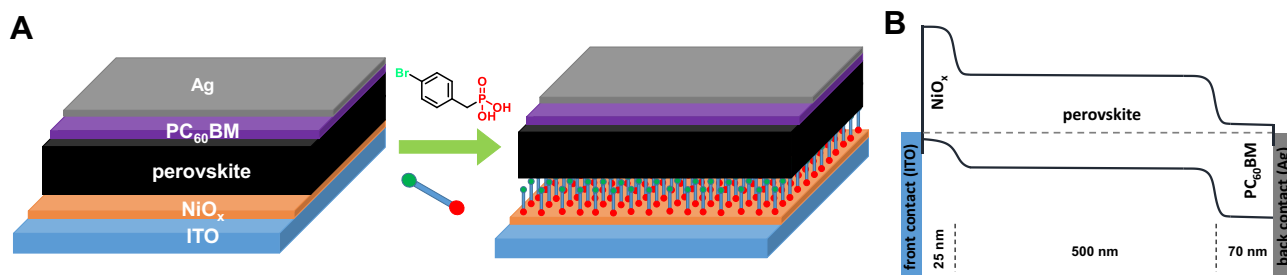


Fig. 1 **a** Schematic illustration of the modification of the NiO_x -layer with 4-bromobenzylphosphonic acid and the device architectures of the investigated solar cells (glass/ITO/ NiO_x /perovskite/ PC_{60}BM /Ag) without and with Br-BPA modification, **b** schematic energy band dia-

gram for the device configuration ITO/ NiO_x /perovskite/ PC_{60}BM /Ag; the scheme is not drawn to scale and the Fermi level is taken as the reference energy level

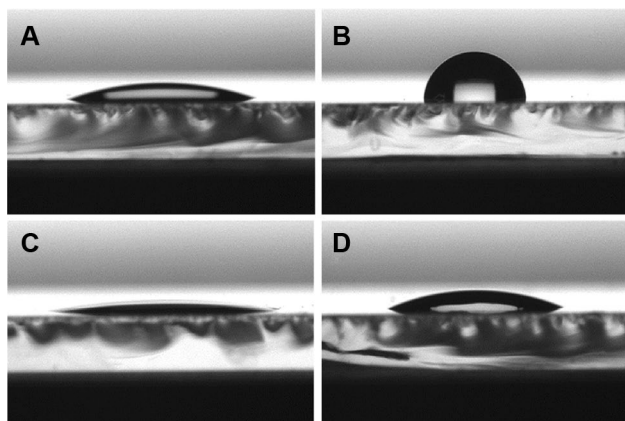


Fig. 2 Images showing the typical drop shapes of **a** water on a NiO_x film, **b** water on a $\text{NiO}_x/\text{Br-BPA}$ film, **c** ethylene glycol on a NiO_x film and **d** ethylene glycol on a $\text{NiO}_x/\text{Br-BPA}$ film

confirmed by contact angle measurements. Figure 2 shows the changes in the shape of water and ethylene glycol drops on the non-modified and modified NiO_x films. The corresponding values of the contact angles are summarized in Table 1. It is apparent that the contact angle of water is significantly increased from 21.9° to 93.1° due to the Br-BPA modification indicating a rise in the hydrophobicity of the surface. The high contact angle of water after the modification also indicates a dense coverage of the NiO_x surface with the Br-BPA molecules. To calculate the surface free energy of the films, additional contact angle measurements with ethylene glycol were performed showing an increase from

15.8° to 24.3° due to the introduction of the Br-BPA SAM. The surface free energy of the NiO_x film was calculated to be 88.4 mN m^{-1} with a very low disperse part of 0.47 mN m^{-1} and a polar part of 88.0 mN m^{-1} . After the modification, a value of 126.5 mN m^{-1} was obtained and the polarity changed completely to a disperse part of 120.9 mN m^{-1} and a polar part of 5.6 mN m^{-1} . This indicates a successful incorporation of the Br-BPA molecules on the surface of the NiO_x layers and the corresponding change in surface properties.

In order to confirm the presence of the phosphonic acid molecules at the surface of the NiO_x film, we performed XPS measurements. The survey XPS spectra of the non-modified and modified NiO_x films are shown in Fig. 3a and b. The high peak intensities of indium (In) and tin (Sn) are indicating that the NiO_x layer is at least in some parts only a few nanometres thin. Due to the high surface sensitivity of this technique, we detect the P 2p doublet of the phosphonic acid at 132.5 eV and the Br 3p doublet at 183 and 190 eV in the modified sample, while these peaks are absent in the reference sample (Fig. 3c). The signal at 284 eV can be assigned to the C 1s peak and is increased with the presence of the SAM molecules.

The corresponding high-resolution XPS core-level spectra are given in the Fig. 3d and e. Peak fits were performed by using a convolution of a Gaussian and a Lorentzian profile.

A quantification of the detectable chemical elements was performed by peak deconvolution of all detailed spectra. In order to get additional information about the surface layers,

Table 1 Results of the contact angle measurements of the non-modified and modified NiO_x layers

Sample	Contact angle—water ($^\circ$)	Contact angle—ethylene glycol ($^\circ$)	Surface free energy (mN m^{-1})	Disperse part (mN m^{-1})	Polar part (mN m^{-1})
NiO_x	21.9 ± 0.3	15.8 ± 2.1	88.4 ± 0.4	0.47 ± 0.03	88.0 ± 0.4
$\text{NiO}_x/\text{Br-BPA}$	93.1 ± 0.3	24.3 ± 0.4	126.5 ± 2.0	120.9 ± 1.6	5.6 ± 0.4

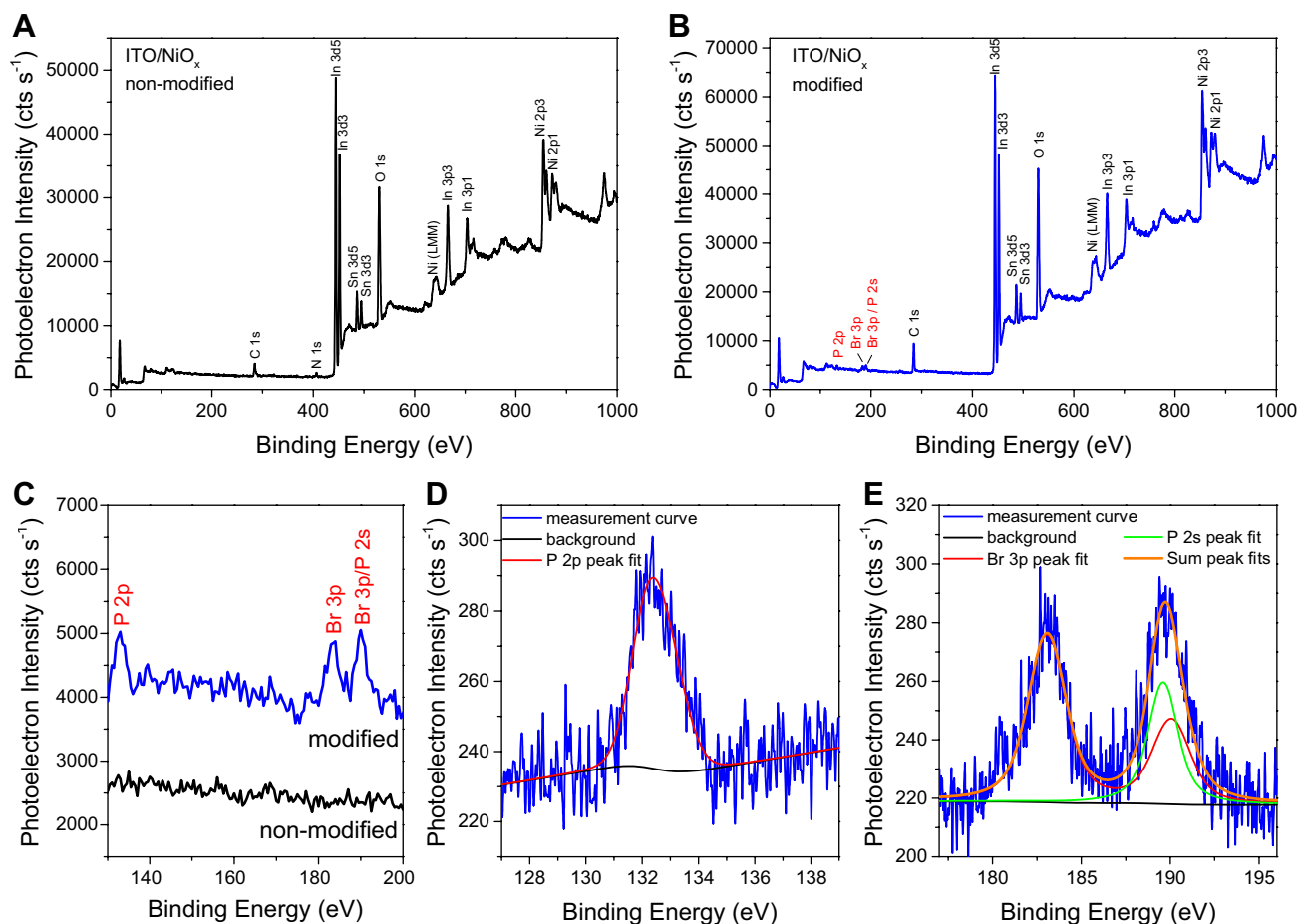


Fig. 3 XPS survey spectra of a non-modified **a** and modified NiO_x film **b**; details of the region of the relevant P- and Br-peaks **c** confirming the presence of phosphor and bromine at the surface of the modi-

fied NiO_x film; high resolution XPS spectra and peak deconvolution of the P 2p **d** and the Br 3p peak with the additional signal of P 2s **e** in the modified sample

XPS spectra were measured under three detection angles of 0°, 35° and 50° relative to the surface normal. As expected, we find increasing signals of surface layers with increasing detection angles. The attenuation of the photoelectron signal (I/I_0) by inelastic scattering in a layer of the thickness (d) can be calculated by using the equation [41]:

$$\frac{I}{I_0} = e^{-\frac{d}{\lambda \cos \theta}} \quad (1)$$

The inelastic mean free path of the photoelectrons (λ) is dependent on the kinetic energy of the photoelectrons and the layer material. The values of λ were determined from the Tanuma, Powell, and Penn TPP2 M formula [42] and the software QUASES written by Sven Tougaard. θ is the detection angle relative to the surface normal. For a given layer system, in our case ITO/NiO_x/Br-BPA, the expected total photoelectron intensity of each element can be calculated by the signal sum over all atomic layers including the atomic density of the element in the layer. The layer model was optimized for the best matching of the calculated

contribution of each element with the element quantification of the measured spectra at all detection angles. We found a good agreement between the measured and calculated data by assumption of a NiO_x nanoparticle layer with an average thickness of around 5 nm on the ITO and a Br-BPA SAM-layer with a density of 4 molecules per nm². This matches well with previously reported surface coverage densities of phosphonic acid molecules on metal oxides [35, 43]. Previous studies on NiO_x HTLs for perovskite solar cells revealed that NiO_x film thicknesses of around 25 nm are beneficial for the solar cell performance. Therefore, we adjusted the thickness of the NiO_x films used in the solar cells in the further course of the study by optimizing the spin coating parameters [10, 11, 15, 31].

In the next step, we investigated the effects of the Br-BPA SAM on the properties of the perovskite thin film. Figure 4a shows the XRD pattern of the Cs_{0.1}(MA_{0.17}FA_{0.83})_{0.9}Pb(I_{0.83}Br_{0.17})₃ perovskite films prepared on non-modified and modified NiO_x films. Both samples show the typical pattern of the cubic perovskite crystal

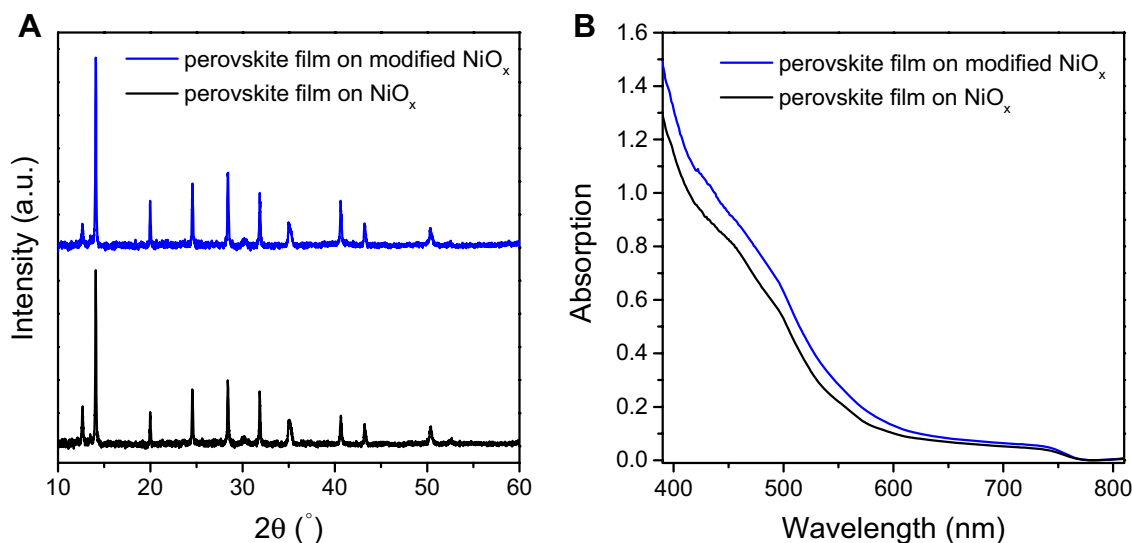


Fig. 4 **a** XRD patterns and **b** UV–Vis absorption spectra of perovskite thin films prepared on glass/ITO/ NiO_x substrates without and with Br-BPA modification

structure with characteristic peaks at 14.1° and 28.4° for the (110) and (220) lattice planes along with peaks at 20.0° , 24.5° , 31.8° , 40.6° and 43.2° 2θ , which matches well with literature data [36, 44, 45]. Furthermore, the intensity ratios of the peaks in the non-modified sample are very similar to the ones in the modified sample indicating no change in orientation of the perovskite crystals relative to the substrate. The peaks at 35.0° and 50.2° 2θ stem from the ITO substrate. The minor peak at 12.7° 2θ indicates small amounts of PbI_2 in the films. A minor excess of PbI_2 was reported to improve the properties of the grain boundaries and to suppress non-radiative charge carrier recombination in the perovskite films [46, 47].

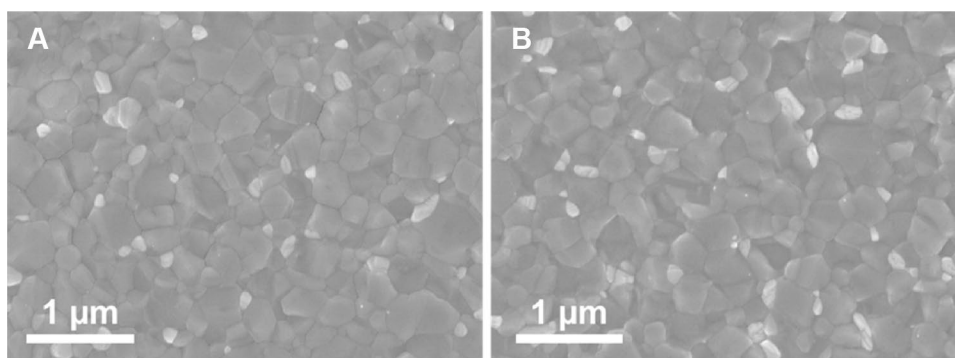
The absorption spectra of the perovskite films suggest a similar absorption onset (~ 770 nm) in agreement with a bandgap of ~ 1.61 eV [36, 45]. The slight differences in the intensity of the absorption spectrum stem from minor changes in the film thickness. The surface profile measurements revealed film thicknesses of the perovskite

layers between 485 and 510 nm independent of the surface modification.

Furthermore, the surface morphology of the perovskite films prepared on glass/ITO/ NiO_x substrates without and with Br-BPA modification was investigated by scanning electron microscopy. The top view images depicted in Fig. 5 reveal homogeneous perovskite films and their complete coverage of the NiO_x films. The grain sizes range from 125 to 135 nm for the smaller sized grains to approximately 475–510 nm for the larger ones and no significant changes based on the surface modification are noticed.

To evaluate the influences of the modification on the photovoltaic performance, solar cells with the device architecture glass/ITO/ NiO_x /perovskite/ PC_{60}BM /Ag (cf. scheme in Fig. 1a) were prepared. A schematic energy band diagram based on the values published in literature [48–51] is shown in Fig. 1b. The Fermi level has been chosen as the reference energy level instead of the vacuum level since this is more suited to describe non-ideal systems such as the herein

Fig. 5 Top view SEM images of perovskite thin films prepared on a non-modified (**a**) and modified (**b**) NiO_x layer



discussed devices [51]. The JV curves of typical solar cells without and with Br-BPA modification measured in fwd and bwd direction are presented in Fig. 6a. The corresponding characteristic parameters are summarized in Table 2. The most obvious change in the photovoltaic properties is the enhanced photovoltage in the devices with the Br-BPA modification. In these solar cells, the V_{OC} is increased from 0.978 V to 1.019–1.029 V. This increase in V_{OC} resonates with previous reports investigating benzoic acids for the NiO_x modification and originates most presumably from the lowering of the valence band energy of the NiO_x films by the surface modification [31]. Moreover, there is a slight increase in short circuit current density (J_{SC}) detectable for the solar cells with Br-BPA modification which can be attributed to the dipole moment of the molecule.

The prepared solar cells exhibit an only minor hysteresis, as can be seen in the JV curves in Fig. 6a. The hysteresis index (HI) of the solar cells was calculated according to

$$HI = \frac{\int_{SC}^{OC} (J_{bwd}(V) - J_{fwd}(V)) dV}{\int_{SC}^{OC} J_{bwd}(V) dV} \quad (2)$$

whereby, $J_{bwd}(V)$ indicates the area of the JV curve for the backward scan and $J_{fwd}(V)$ indicates the area for the forward scan in the region between short circuit (SC) and open circuit (OC) conditions. This equation was adapted from Ref.

[52] which considers the integrated power output of the solar cells in fwd (SC to OC) and bwd (OC to SC) scan directions. Based on Nemnes et al. [53–55] this method is useful for the determination of the HI for normal and inverted hysteresis in non-crossing JV curves. If the HI approaches 0, the solar cell would have negligible hysteresis. For the typical solar cells shown, we calculated an HI of -0.0562 for the device with the non-modified NiO_x layer and the HI is slightly reduced to -0.0131 for the solar cell with the modified NiO_x HTL.

The MPP tracking measurements (Fig. 6b) reveal a constant power output of the solar cells. While the voltage at the MPP (V_{MPP}) is slightly decreasing at the beginning of the measurement, the current density at the MPP (J_{MPP}) improves slightly leading to a constant power output and a PCE of 11.4% and 12.2% for the non-modified and the modified device after 10 min of continuous illumination, respectively.

The EQE spectra (Fig. 6c) for the representative devices show a typical shape of perovskite solar cells with an onset at 770 nm and a characteristic plateau at wavelengths below 750 nm. Moreover, the spectra remain almost unchanged upon the modification of the NiO_x HTL. This is expected, as the J_{SC} for the representative devices are rather similar. The integrated J_{SC} calculated from the EQE spectrum sums up to 18.2 and 18.4 mA/cm^2 and is within a few percent deviation to the values extracted from the JV curves.

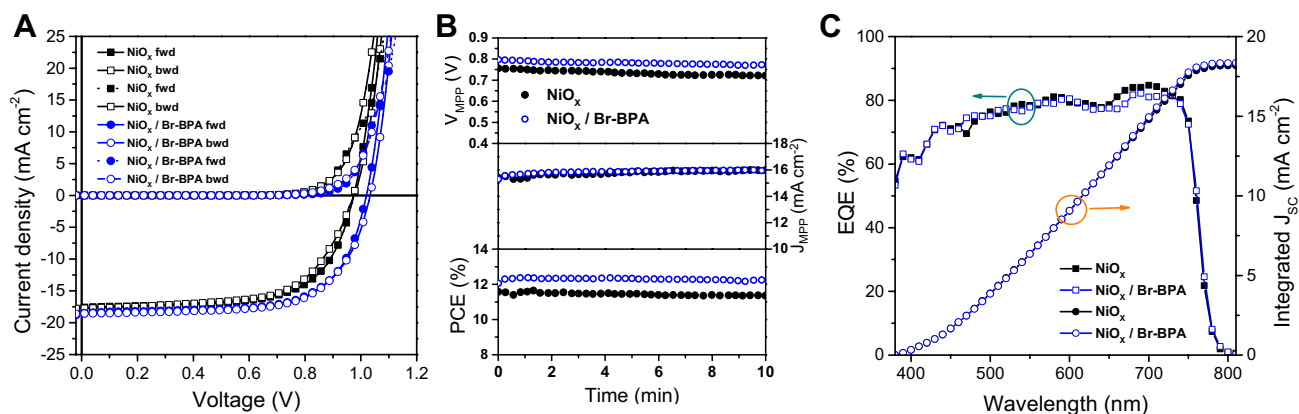


Fig. 6 **a** JV curves (dark and illuminated) measured in forward and backward direction, **b** maximum power point tracking measurements and **c** EQE spectra of typical perovskite solar cells prepared with non-modified and modified NiO_x hole transport layers

Table 2 Characteristic parameters of typical perovskite solar cells prepared with non-modified and modified NiO_x hole transport layers

	Scan direction	V_{OC} (V)	J_{SC} ($mA\ cm^{-2}$)	FF (%)	PCE (%)	R_S (Ωcm^2)	R_{SH} (Ωcm^2)	HI
NiO_x	bwd	0.978	17.77	62.69	10.82	8.13	645	-0.0562
	fwd	0.978	17.68	65.04	11.16	5.14	970	
$NiO_x/Br-BPA$	bwd	1.029	18.58	67.18	12.73	4.68	1240	-0.0131
	fwd	1.019	18.57	66.94	12.54	4.29	751	

The statistical data of the 20 best solar cells (non-modified and modified separately) prepared within this study are shown using box plots in Fig. 7. These data support the discussion above. Figure 7 reveals that the V_{OC} of the solar cells is enhanced in both scan directions; also the average J_{SC} is slightly improved. Regarding the fill factor (FF), there is no major change observed. This results in an average increase in PCE from $11.4 \pm 0.7\%$ ($11.1 \pm 1.1\%$) to $12.1 \pm 0.3\%$ ($12.6 \pm 0.3\%$) for the Br-BPA modification based solar cells in fwd (bwd) scan directions, respectively.

With the Br-BPA modification, we observed V_{OC} s of up to 1.1 V in this study. The JV curves of such a solar cell are shown in Fig. 8. In bwd scan direction a V_{OC} of 1.099 V was obtained corroborating the potential of this modification strategy. The EQE spectrum reveals values up to 87.9% and the derived integrated J_{SC} (19.55 mA cm^{-2}) shows consistency with the J_{SC} observed in the JV curve. The PCE of this solar cell was at 12.7%.

4 Conclusions

In summary, we successfully functionalized solution processed NiO_x HTLs by a dip coating procedure using a Br-BPA solution in acetonitrile. This is substantiated by the markedly increased contact angle of water, the surface free energies and the detection of P 2p and Br 3p peaks in the modified sample by XPS measurements. We did not observe any notable change in the optical properties and surface morphology of the perovskite layers. However, the JV curves reflect improved photovoltaic performance, particularly an increased V_{OC} . A typical device shows an improved PCE from 11.2% (10.8%) to 12.5% (12.7%) due to an improved V_{OC} from 0.978 V (0.978 V) to 1.019 V (1.029 V) in fwd (bwd) scan directions, respectively. We assume that the improvement in the V_{OC} is largely due to the realignment of the energy levels based on the dipole

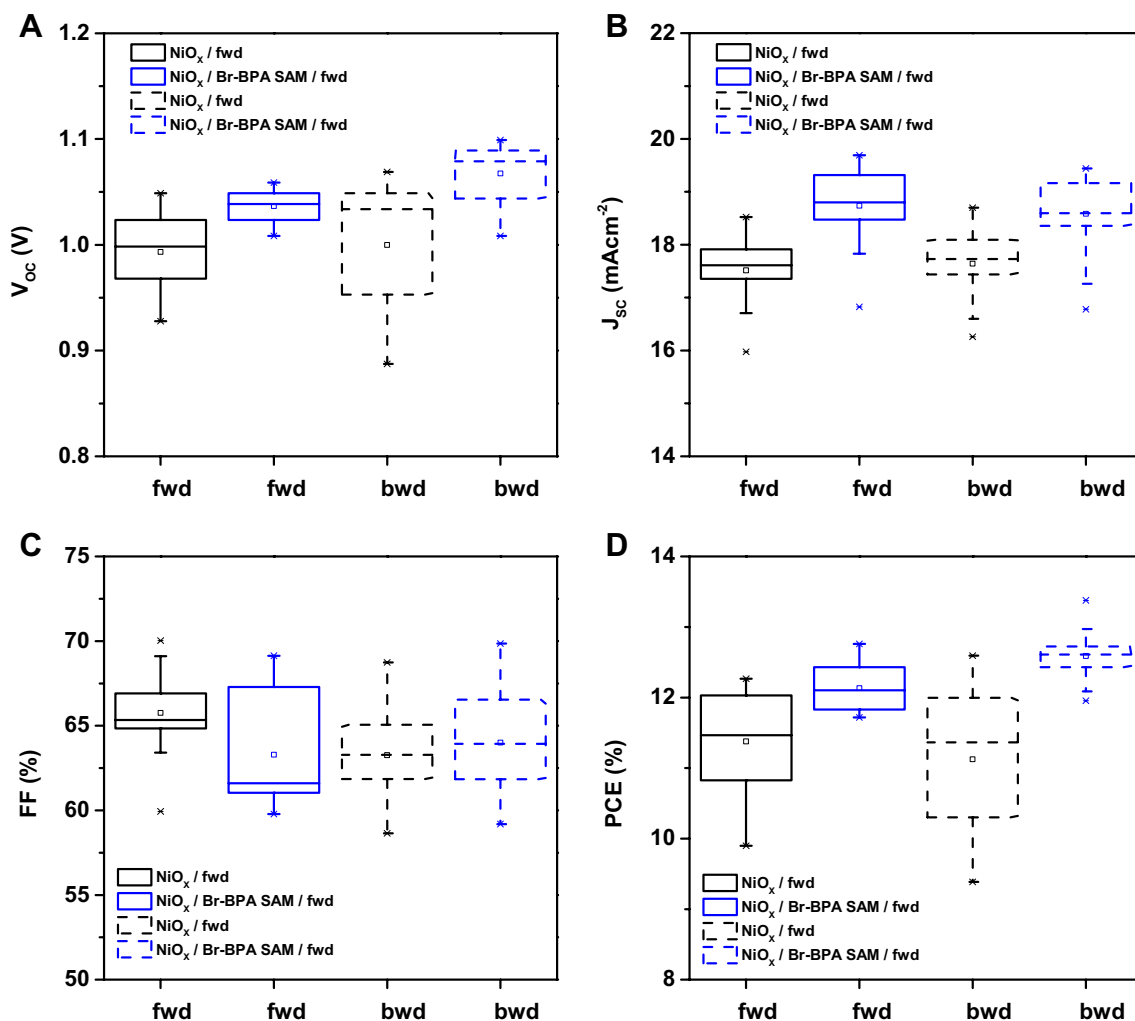


Fig. 7 Box plots showing statistics of the characteristic parameters **a** V_{OC} , **b** J_{SC} , **c** FF and **d** PCE of the best 20 devices prepared each with non-modified and modified NiO_x hole transport layers

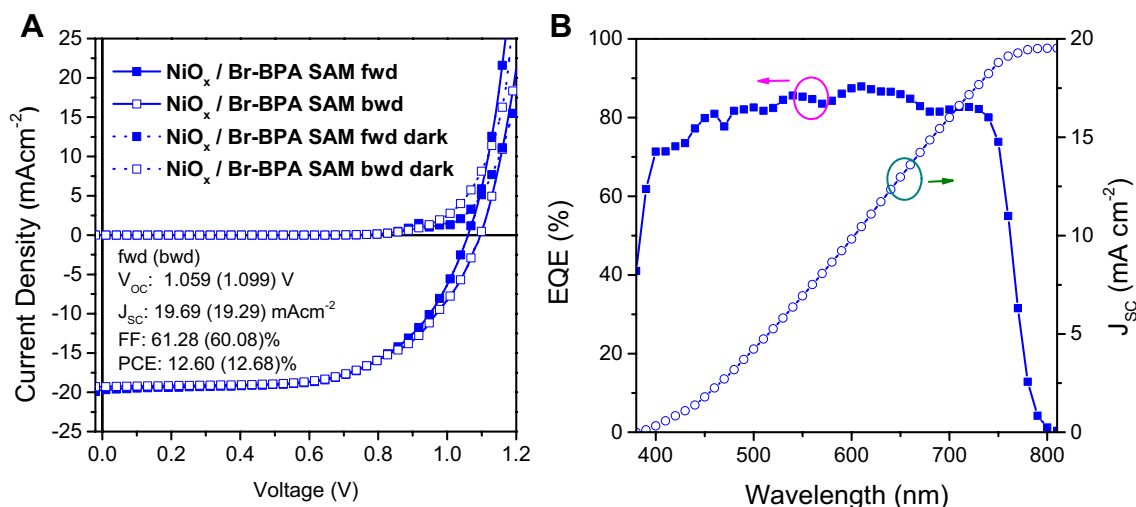


Fig. 8 JV curves (a) and EQE spectrum (b) of one of the devices with Br-BPA modification showing the highest V_{oc} prepared within this study

moment of the Br-BPA SAM molecules. With devices having Br-BPA modifications, V_{oc} s of up to 1.099 V could be obtained. Furthermore, MPP tracking measurements revealed a steady state PCE of 11.35% and 12.22% for typical devices without and with Br-BPA modified NiO_x films.

Acknowledgements Open access funding provided by Graz University of Technology. This work was carried out within the project “flex!PV_2.0” (FFG No. 853603) funded by the Austrian Climate and Energy Fund within the program Energy Emission Austria. Birgit Ehmman is gratefully acknowledged for experimental support.

Open Access This article is distributed under the terms of the Creative Commons Attribution 4.0 International License (<http://creativecommons.org/licenses/by/4.0/>), which permits unrestricted use, distribution, and reproduction in any medium, provided you give appropriate credit to the original author(s) and the source, provide a link to the Creative Commons license, and indicate if changes were made.

References

- N.J. Jeon, H. Na, E.H. Jung, T.-Y. Yang, Y.G. Lee, G. Kim, H.-W. Shin, S.I. Seok, J. Lee, J. Seo, *Nature Energy* **3**, 682–689 (2018)
- <https://www.nrel.gov/pv/assets/pdfs/best-research-cell-efficiency.pdf>
- M.A. Green, Y. Hishikawa, E.D. Dunlop, D.H. Levi, J. Hohl-Ebinger, M. Yoshita, A.W.Y. Ho-Baillie, *Prog. Photovolt. Res. Appl.* **27**, 3–12 (2019)
- W. Chen, Y. Wu, J. Fan, A.B. Djurišić, F. Liu, H.W. Tam, A. Ng, C. Surya, W.K. Chan, D. Wang, Z.-B. He, *Adv. Energy Mater.* **8**, 1703519 (2018)
- S. Ye, H. Rao, Z. Zhao, L. Zhang, H. Bao, W. Sun, Y. Li, F. Gu, J. Wang, Z. Liu, Z. Bian, C. Huang, *J. Am. Chem. Soc.* **139**, 7504–7512 (2017)
- L. Hu, K. Sun, M. Wang, W. Chen, B. Yang, J. Fu, Z. Xiong, X. Li, X. Tang, Z. Zang, S. Zhang, L. Sun, M. Li, *ACS Appl. Mater. Interfaces* **9**, 43902–43909 (2017)
- G. Adam, M. Kaltenbrunner, E.D. Glowacki, D.H. Apaydin, M.S. White, H. Heilbrunner, S. Tombe, P. Stadler, B. Ernecker, C.W. Klampfl, N.S. Sariciftci, M.C. Scharber, *Sol. Energy Mater. Sol. Cells* **157**, 318–325 (2016)
- P.-K. Kung, M.-H. Li, P.-Y. Lin, Y.-H. Chiang, C.-R. Chan, T.-F. Guo, P. Chen, *Adv. Mater. Interfaces* **5**, 1800882 (2018)
- M.D. Irwin, D.B. Buchholz, A.W. Hains, R.P.H. Chang, T.J. Mark, *Proc. Natl. Acad. Sci.* **105**, 2783–2787 (2008)
- W. Chen, F.-Z. Liu, X.-Y. Feng, A.B. Djurišić, W.K. Chan, Z.-B. He, *Adv. Energy Mater.* **7**, 1700722 (2017)
- H.-S. Kim, J.-Y. Seo, H. Xie, M. Lira-Cantu, S.M. Zakeeruddin, M. Grätzel, A. Hagfeldt, *ACS Omega* **2**, 9074–9079 (2017)
- J. Zheng, L. Hu, J.S. Yun, M. Zhang, C.F.J. Lau, J. Bing, X. Deng, Q. Ma, Y. Cho, W. Fu, C. Chen, M.A. Green, S. Huang, A.W.Y. Ho-Baillie, *ACS Appl. Energy Mater.* **1**, 561–570 (2018)
- J.H. Kim, P.-W. Liang, S.T. Williams, N. Cho, C.-C. Chueh, M.S. Glaz, D.S. Ginger, A.K.-Y. Jen, *Adv. Mater.* **27**, 695–701 (2015)
- Z. Liu, A. Zhu, F. Cai, L. Tao, Y. Zhou, Z. Zhao, Q. Chen, Y.-B. Cheng, H. Zhou, *J. Mater. Chem. A* **5**, 6597–6605 (2017)
- S. Weber, T. Rath, J. Mangalam, B. Kunert, A.M. Coclite, M. Bauch, T. Dimopoulos, G. Trimmel, *J. Mater. Sci.: Mater. Electron.* **29**, 1847–1855 (2018)
- X. Yin, Z. Yao, Q. Luo, X. Dai, Y. Zhou, Y. Zhang, Y. Zhou, S. Luo, J. Li, N. Wang, H. Lin, *ACS Appl. Mater. Interfaces* **9**, 2439–2448 (2017)
- S.S. Mali, H. Kim, S.E. Shim, C.K. Hong, *Nanoscale* **8**, 19189–19194 (2016)
- Z. Zhu, Y. Bai, T. Zhang, Z. Liu, X. Long, Z. Wei, Z. Wang, L. Zhang, J. Wang, F. Yan, S. Yang, *Angew. Chem. Int. Ed.* **53**, 12571–12575 (2014)
- J.W. Jung, C.-C. Chueh, A.K.-Y. Jen, *Adv. Mater.* **27**, 7874–7880 (2015)
- J.H. Park, J. Seo, S. Park, S.S. Shin, Y.C. Kim, N.J. Jeon, H.-W. Shin, T.K. Ahn, J.H. Noh, S.C. Yoon, C.S. Hwang, S.I. Seok, *Adv. Mater.* **27**, 4013–4019 (2015)
- K.-C. Wang, P.-S. Shen, M.-H. Li, S. Chen, M.-W. Lin, P. Chen, T.-F. Guo, *ACS Appl. Mater. Interfaces* **6**, 11851–11858 (2014)

22. A.S. Subbiah, A. Halder, S. Ghosh, N. Mahuli, G. Hodes, S.K. Sarkar, *J. Phys. Chem. Lett.* **5**, 1748–1753 (2014)
23. S. Seo, I.J. Park, M. Kim, S. Lee, C. Bae, H.S. Jung, N.-G. Park, J.Y. Kim, H. Shin, *Nanoscale* **8**, 11403–11412 (2016)
24. Y. Hou, W. Chen, D. Baran, T. Stubhan, N.A. Luechinger, B. Hartmeier, M. Richter, J. Min, S. Chen, C.O.R. Quiroz, N. Li, H. Zhang, T. Heumueller, G.J. Matt, A. Osvet, K. Forberich, Z.-G. Zhang, Y. Li, B. Winter, P. Schweizer, E. Spiecker, C.J. Brabec, *Adv. Mater.* **28**, 5112–5120 (2016)
25. S. Seo, S. Jeong, H. Park, H. Shin, N.-G. Park, *Chem. Commun.* **55**, 2403–2416 (2019)
26. A. Abrusci, S.D. Stranks, P. Docampo, H.L. Yip, A.K.-Y. Jen, H.J. Snaith, *Nano Lett.* **13**, 3124–3128 (2013)
27. L. Zuo, Z. Gu, T. Ye, W. Fu, G. Wu, H. Li, H. Chen, *J. Am. Chem. Soc.* **137**, 2674–2679 (2015)
28. L. Yang, G. Chen, Y. Sun, D. Han, S. Yang, M. Gao, P. Zou, H. Luan, X. Kong, J. Yang, *Electrochim. Acta* **164**, 38–47 (2015)
29. P. Zhao, B.J. Kim, H.S. Jung, *Mater. Today Energy* **7**, 267–286 (2018)
30. R. Azmi, W.T. Hadmojo, S. Sinaga, C.-L. Lee, S.C. Yoon, I.H. Jung, S.-Y. Jang, *Adv. Energy Mater.* **8**, 1701683 (2018)
31. Q. Wang, C.-C. Chueh, T. Zhao, J. Cheng, M. Eslamian, W.C.H. Choy, A.K.-Y. Jen, *ChemSusChem* **10**, 3794–3803 (2017)
32. S.A. Paniagua, A.J. Giordano, O.N.L. Smith, S. Barlow, H. Li, N.R. Armstrong, J.E. Pemberton, J.-L. Brédas, D. Ginger, S.R. Marder, *Chem. Rev.* **116**, 7117–7158 (2016)
33. I. Lange, S. Reiter, J. Kniepert, F. Piersimoni, M. Pätz, J. Hildebrandt, T. Brenner, S. Hecht, D. Neher, *Appl. Phys. Lett.* **106**, 113302 (2015)
34. I. Lange, S. Reiter, M. Pätz, A. Zykov, A. Nefedov, J. Hildebrandt, S. Hecht, S. Kowarik, C. Wöll, G. Heimel, D. Neher, *Adv. Funct.* **24**, 7014–7024 (2014)
35. C. Wood, H. Li, P. Winget, J.-L. Brédas, *J. Phys. Chem. C* **116**, 19125–19133 (2012)
36. M. Saliba, T. Matsui, J.-Y. Seo, K. Domanski, J.-P. Correa-Baena, M.K. Nazeeruddin, S.M. Zakeeruddin, W. Tress, A. Abate, A. Hagfeldt, M. Grätzel, *Energy Environ. Sci.* **9**, 1989–1997 (2016)
37. H. Zhang, J. Cheng, F. Lin, H. He, J. Mao, K.S. Wong, A.K.-Y. Jen, W.C.H. Choy, *ACS Nano* **10**, 1503–1511 (2016)
38. F. Jiang, W.C.H. Choy, X. Li, D. Zhang, J. Cheng, *Adv. Mater.* **27**, 2930–2937 (2015)
39. X. Yin, P. Chen, M. Que, Y. Xing, W. Que, C. Niu, J. Shao, *ACS Nano* **10**, 3630–3636 (2016)
40. D.K. Owens, R.C. Wendt, *J. Appl. Polym. Sci.* **13**, 1741–1747 (1969)
41. D. Briggs, M.P. Seah (eds.), *Practical Surface Analysis (Second Edition) Volume 1: Auger and X-ray Photoelectron Spectroscopy* (Wiley, Hoboken, 1990), p. 183
42. S. Tanuma, C.J. Powell, D.R. Penn, *Surf. Interf. Anal.* **21**, 165–176 (1993)
43. R. Luschtinetz, A.F. Oliveira, J. Frenzel, J.-O. Joswig, G. Seifert, H.A. Duarte, *Surf. Sci.* **602**, 1347–1359 (2008)
44. T. Singh, T. Miyasaka, *Adv. Energy Mater.* **8**, 1700677 (2018)
45. M. Saliba, T. Matsui, K. Domanski, J.-Y. Seo, A. Ummadisingu, S.M. Zakeeruddin, J.-P. Correa-Baena, W.R. Tress, A. Abate, A. Hagfeldt, M. Grätzel, *Science* **354**, 206–209 (2016)
46. T.J. Jacobsson, J.-P. Correa-Baena, E.H. Anaraki, B. Philippe, S.D. Stranks, M.E.F. Bouduban, W. Tress, K. Schenk, J. Teuscher, J.-E. Moser, H. Rensmo, A. Hagfeldt, *J. Am. Chem. Soc.* **138**, 10331–10343 (2016)
47. D. Bi, W. Tress, M.I. Dar, P. Gao, J. Luo, C. Renevier, K. Schenk, A. Abate, F. Giordano, J.-P. Correa-Baena, J.-D. Decoppet, S.M. Zakeeruddin, M.K. Nazeeruddin, M. Grätzel, A. Hagfeldt, *Sci. Adv.* **2**, e1501170 (2016)
48. C.-C. Chueh, C.-Z. Li, A.K.-Y. Jen, *Energy Environ. Sci.* **8**, 1160–1189 (2015)
49. M. Deepa, M. Salado, L. Calio, S. Kazim, S.M. Shivaprasad, S. Ahmad, *Phys. Chem. Chem. Phys.* **19**, 4069–4077 (2017)
50. B. de Boer, A. Hadipour, M.M. Mandoc, T. van Woudenberg, P.W.M. Blom, *Adv. Mater.* **17**, 621–625 (2005)
51. I.M. Dharmadasa, Y. Rahaq, A.A. Ojo, T.I. Alanazi, *J. Mater. Sci.: Mater. Electron.* **30**, 1227–1235 (2019)
52. J.-W. Lee, S.-G. Kim, S.-H. Bae, D.-K. Lee, O. Lin, Y. Yang, N.-G. Park, *Nano Lett.* **17**, 4270–4276 (2017)
53. G.A. Nemnes, C. Besleaga, V. Stancu, D.E. Dograu, L.N. Leonat, L. Pintilie, K. Torfason, M. Ilkov, A. Manolescu, I. Pintilie, *J. Phys. Chem. C* **121**, 11207–11214 (2017)
54. G.A. Nemnes, C. Besleaga, A.G. Tomulescu, A. Palici, L. Pintilie, A. Manolescu, I. Pintilie, *Sol. Energy* **173**, 976–983 (2018)
55. G.A. Nemnes, C. Besleaga, A.G. Tomulescu, L.N. Leonat, V. Stancu, M. Florea, A. Manolescu, I. Pintilie, *J. Mater. Chem. C* (2019). <https://doi.org/10.1039/c8tc05999c>

Publisher's Note Springer Nature remains neutral with regard to jurisdictional claims in published maps and institutional affiliations.